PSFC/JA-08-49

Role of zonal flows in trapped electron mode turbulence through nonlinear gyrokinetic particle and continuum simulation

Ernst, D. R.; Lang, J.[1]; Nevins, W. M.[2];
Hoffman, M.[3]; Chen, Y.[1]; Dorland, W.[4]; Parker, S.[1]

June 2009

Plasma Science and Fusion Center
Massachusetts Institute of Technology
Cambridge MA 02139 USA

[1]University of Colorado, Boulder
[2]Lawrence Livermore National Laboratory
[3]Missouri University of Science and Technology
[4]University of Maryland

This work was supported in part by the U.S. Department of Energy, Grant No. DE-FG02-91ER-54109.

Role of zonal flows in trapped electron mode turbulence through nonlinear gyrokinetic particle and continuum simulation*

D. R. Ernst†
Plasma Science and Fusion Center
Massachusetts Institute of Technology
167 Albany Street, NW16-258
Cambridge, Massachusetts 02139

J. Lang, Y. Chen, and S. Parker
Center for Integrated Plasma Studies, Univ. of Colorado, Boulder, Colorado

W. M. Nevins
Lawrence Livermore National Laboratory, Livermore, California

M. Hoffman
Depts. of Physics and Nuclear Engineering, Missouri University of Science and Technology, Rolla, Missouri

W. Dorland
Dept. of Physics, IREAP & CSCAMM, Univ. of Maryland, College Park, Maryland
(Dated: January 5, 2009)

Trapped electron mode (TEM) turbulence exhibits a rich variety of collisional and zonal flow physics. This work explores the parametric variation of zonal flows and underlying mechanisms through a series of linear and nonlinear gyrokinetic simulations, using both particle-in-cell and continuum methods. A new stability diagram for electron modes is presented, identifying a critical boundary at $\eta_e = 1$, separating long and short wavelength TEMs. A novel parity test is used to separate TEMs from electron temperature gradient driven modes. A nonlinear scan of η_e reveals fine scale structure for $\eta_e \gtrsim 1$, consistent with linear expectation. For $\eta_e < 1$, zonal flows are the dominant saturation mechanism, and TEM transport is insensitive to η_e. For $\eta_e > 1$, zonal flows are weak, and TEM transport falls inversely with a power law in η_e. The role of zonal flows appears to be connected to linear stability properties. Particle and continuum methods are compared in detail over a range of $\eta_e = d\ln T_e/d\ln n_e$ values from zero to five. Linear growth rate spectra, transport fluxes, fluctuation wavelength spectra, zonal flow shearing spectra, and correlation lengths and times are in close agreement. In addition to identifying the critical parameter η_e for TEM zonal flows, this paper takes a challenging step in code verification, directly comparing very different methods of simulating simultaneous kinetic electron and ion dynamics in TEM turbulence.

PACS numbers: 52.25.Fi,52.25.Vy,52.30.Gz,52.35.Kt,52.35.Ra,52.50.Qt, 52.55.Dy,52.55.Fa,52.65.Tt

I. INTRODUCTION

Trapped electron mode (TEM) turbulence is relevant to particle and electron thermal energy transport. Several types of TEMs exist, driven by either the electron density gradient, or by the electron temperature gradient. The most significant modes are associated with non-resonant "bad curvature" drive as well as trapped electron toroidal precession drift resonance. It is essential to retain the ion magnetic curvature and ∇B drifts as well as those of the trapped electrons. TEM turbulence is most relevant when toroidal ion temperature gradient driven (ITG) modes are either stable or weakly unstable. This scenario arises in a variety of contexts, such as internal transport barriers, cases with strong density peaking, cases with $T_e > T_i$, and low density regimes in which confinement scales favorably with density. It is important to understand the mechanisms underlying particle and electron thermal energy transport for future devices such as ITER [1], where core fueling is greatly reduced, and electrons are heated directly by α-particles. TEM turbulence is of particular interest in scenarios with primarily electron heating [2, 3]. In Alcator C-Mod [4] ITB plasmas, TEM turbulence produces strong particle and electron thermal energy transport as the density and electron temperature gradients increase [5]. This enables ITBs to be controlled externally by central ion cyclotron resonance heating [6]. Further, in a first of its kind comparison, using a new synthetic diagnostic, nonlinear gyrokinetic simulations of TEM turbulence have closely reproduced the measured wavelength spectrum of density fluctuations in an ITB experiment in which TEMs were predicted to be the dominant instability [6].

Recent work on TEM turbulence has resulted in an

*Paper YI2.3, Bull. Am. Phys. Soc. **53**(14), 323 (2008). This paper has been published in Physics of Plasmas **16**, 055906 (2009).
†Electronic address: dernst@psfc.mit.edu

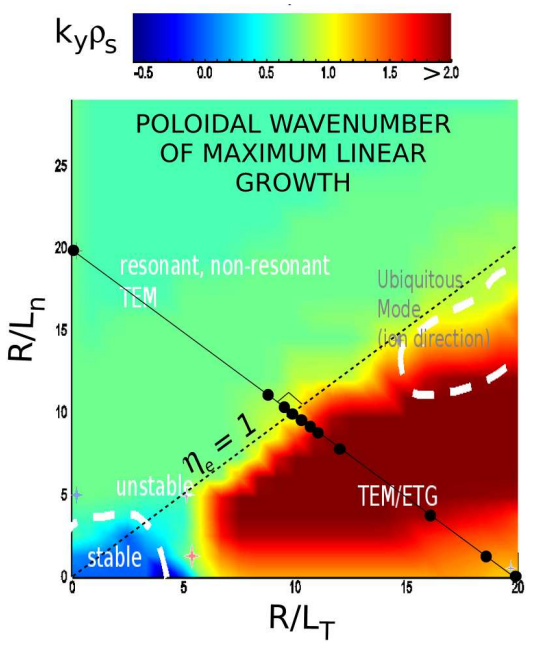

FIG. 1: (Color) Stability diagram for electron modes ($\nabla T_i = 0$). Threshold for ETG modes is $\eta_e = 1.2$ (not shown). Diagram shows binormal (∼poloidal) wavenumber of maximum growth rate. The region bordered in white for $R/L_T > 15$ corresponds to "ubiquitous" modes, defined here as those modes propagating in the ion diamagetic direction.

apparent contradiction regarding the role of zonal flows. Initial studies revealed a new nonlinear upshift of the TEM critical density gradient [5], in which zonal flows were clearly important. In these purely density gradient driven cases, the role of secondary instability is evident in the creation of zonal flow dominated, quasi-steady states in the upshift regime. The upshift increases strongly with collisionality [6], consistent with the strong damping of TEMs by electron detrapping, and the relatively weak ion collisional damping of zonal flows. In contrast, zonal flows were shown to have little effect on the TEM saturation level in cases with strong electron temperature gradients and $T_e = 3T_i$ [7]. This apparent contradiction was addressed by work that bridged the two regimes [8, 9]. The importance of zonal flows in TEM turbulence was found to vary with ∇T_e, T_e/T_i, and magnetic shear [8, 10]. A simplified and qualitative fluid linear and wave-kinetic nonlinear model [11] of the TEM zonal flow growth rate, neglecting ion dynamics and density gradient driven TEMs, finds a weaker zonal flow growth rate at larger η_e. However, a strong resonant behavior near the threshold for the temperature gradient driven mode is shown in Ref. [11], but not observed in our simulations.

When zonal flows are not the dominant saturation mechanism, a simple mode coupling model has been constructed [10], consisting of the dominant primary instability, its damped complex conjugate, and the marginally stable zonal mode. In this model, otherwise stable density fluctuations, with poloidal wavenumbers $k_y = 0$, are driven to large amplitudes at twice the growth rate of the dominant "primary" mode. The zonal fluctuations saturate the primary via $E \times B$ nonlinearity. Simple estimates of the saturation level are obtained, which qualitatively agree with the GEM simulations in the early phase of saturation [10]. Similar ideas were proposed in rich detail in Refs. [12–14], although using a slab model of the dissipative (collisionally destabilized) TEM, less relevant to our study. The details of the latter work rely on wave frequencies exceeding growth rates, which are due to collisions. In contrast, the toroidal modes we study are often very low frequency, and can be purely growing at shorter wavelengths. Nevertheless, the methods and insights in Refs. [14], particularly calculations of spectral transfer rates that strongly favor zonal modes, could prove fruitful. In the comparisons between the simple model of Ref. [10] with simulations, linear growth rates are obtained numerically and retain the ion and electron magnetic curvature and ∇B drifts. A four wave mode coupling model for zonal flow drive [15] was proposed earlier, but did not consider damped eigenmodes. We also point out that when zonal flows are strong, particularly in the nonlinear upshift regime, secondary or modulational instability [16, 17] appears highly relevant, and is observed in the simulations [6].

The weak role of zonal flows for large T_e/T_i and strong electron temperature gradients was exploited in a quasilinear TEM model described most recently in Ref. [18], which also suggests, very differently, that TEMs saturate as a result of their own particle diffusivity. An earlier model suggested TEMs saturate as a result of their own thermal conductivity [19] (see Eq. (4)). Our results suggest that these models would be relevant only if $\eta_e > 1$ (for $T_e = T_i$ and similar values of the other parameters in this study), apart from the strong coupling to zonal modes and damped modes identified in Refs. [10, 14].

To establish a connection between zonal flows and plasma parameters, we begin with a detailed linear stability analysis of electron modes. The results of this stability analysis suggest η_e is an important parameter with a critical value near unity. Based on the linear results, we construct a scan of η_e along a line normal to $\eta_e = 1$, with fine increments where rapid changes in the linear spectrum are observed (see Fig. 1). We consider the "Cyclone Base Case" [20], idealized from a DIII-D (Doublet III-D) L-Mode plasma ($r/R_0 = 0.18$, $q = 1.4$, $T_e = T_i$, $r/qdq/dr = 0.8$). To study electron modes and avoid ITG modes, we maintain zero ion temperature gradient for all cases, and scan the electron temperature and density gradients with all other parameters fixed. Continuum simulations in this paper are performed using the 8/17/2004 version of the GS2 code [21], while particle simulations are performed using the GEM flux tube code [22].

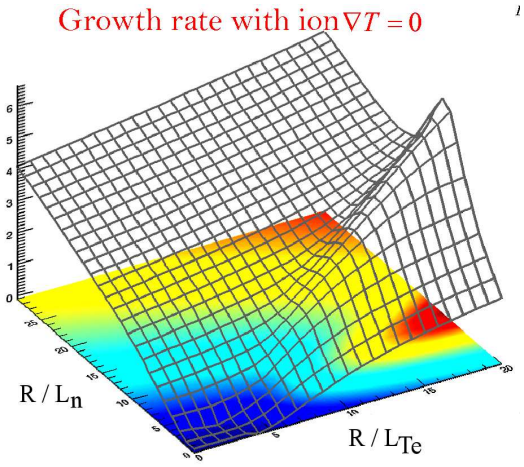

FIG. 2: (Color) Growth rate in units of R_0/c_s as a function of driving gradients, corresponding to Fig. 1. For $\eta_e \gtrsim 1$, the density gradient is stabilizing, while it is destabilizing for $\eta_e < 1$ and $\eta_e \gg 1$.

II. LINEAR STABILITY ANALYSIS

Using over 2,000 linear GS2 simulations, each sweeping the poloidal (binormal) wavenumber $0 < k_y\rho_s < 4$, we have constructed a new and detailed stability diagram for electron modes as a function of their driving gradients, keeping zero ion temperature gradient. Here $\rho_s = c_s/\Omega_i$ with sound speed $c_s^2 = T_e/m_i$ and Ω_i the ion cyclotron frequency. The y-direction (referred to here as "binormal" or "poloidal") is normal to a given magnetic field line and tangent to the magnetic flux surface, while the x-direction is normal to the magnetic flux surface, i.e., in the direction of increasing minor radius ("radial"). The two codes utilize Clebsh cooordinates, where the magnetic field $\mathbf{B} = \nabla\alpha \times \nabla\psi$, with $\alpha = \zeta - q(\psi)\theta$, where $x \propto \psi$ labels the flux surface, q is the magnetic safety factor, $y \propto \alpha$ labels the magnetic field line within a flux surface, and $z \propto \theta$ is the distance along the field line, projected as an angle on the poloidal plane. Figure 1 shows the poloidal wavenumber of maximum growth as a function of the driving factors, the inverse gradient scale lengths for density and temperature, $R/L_n = -R\,d\ln n/dr$ and $R/L_{Te} = -R\,d\ln T_e/dr$, where (R, r) is the (major, minor) radius. Figure 2 shows the maximum linear growth rate as a function of driving gradients, corresponding to Fig. 1.

For $\eta_e < 1$, the linear growth rate spectrum peaks for $k_y\rho_s < 1$, while a sharp transition to short wavelengths $k_y\rho_s > 2$ occurs for $\eta_e \gtrsim 1$. To determine whether Electron Temperature Gradient (ETG) driven modes are responsible for this sudden shift to shorter wavelengths at the $\eta_e = 1$ boundary, we created separate diagrams for modes having even and odd parities with respect to the magnetic field minimum (outer midplane). For frequencies $\omega < \bar{\omega}_{be}$ (the average electron bounce frequency), trapped electrons average odd parity potential

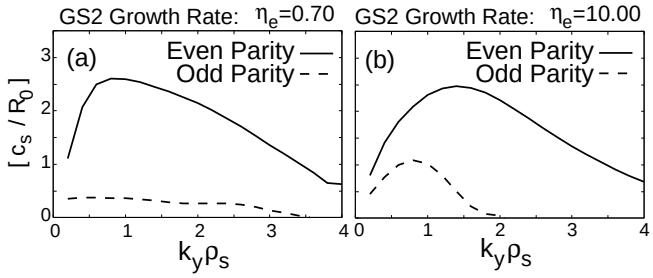

FIG. 3: (a) Growth rate spectra for even and odd parity modes for $\eta_e = 0.70$, and (b) for $\eta_e = 10$.

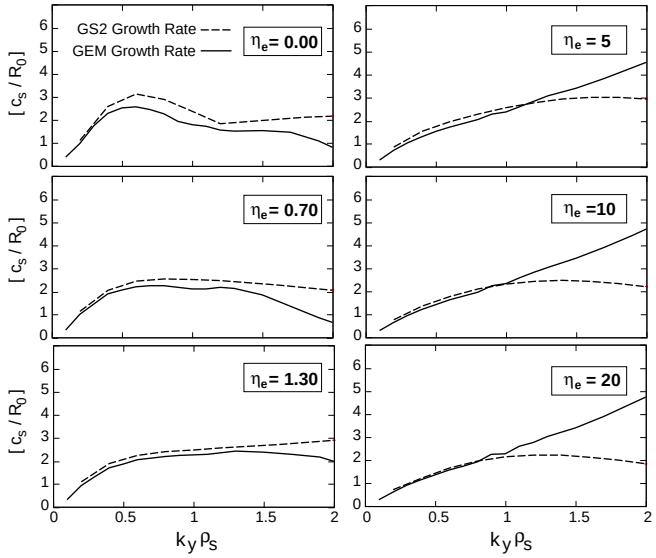

FIG. 4: Comparison of GEM and GS2 linear growth rate spectra for $\eta_e = 0, 0.7, 1.3, 5, 10, 20$, as a function of binormal (∼poloidal) wavenumber $k_y\rho_s = k_\alpha\rho_s$.

fluctuations to zero [23]. Therefore, odd parity modes cannot be driven by trapped electrons. However, ETG modes can be odd or even parity. We expect odd parity ETG modes to be only slightly weaker than even parity ETG modes as a result of more favorable average magnetic curvature and increased parallel Landau damping. However, we find odd parity modes much weaker than even parity modes in all cases, suggesting that trapped electrons are the main destabilizing influence in the parameter ranges considered.

A comparison of linear growth rates and frequencies from GS2, for even and odd parities, is shown in Fig. 3. Odd modes are very weak for $\eta_e < 1$, and weak for $\eta_e > 1$, suggesting that trapped electrons play a strong role even where ETG modes should be unstable for $\eta_e > 1$. Further, the odd parity modes shown are unstable only for $k_y\rho_s < 3.5$ and $k_y\rho_s < 2$, respectively. Note that for $k_y\rho_s \gg 1$, the collisionless TEM becomes fluid-like (does not depend on mode-particle resonances), and the most unstable modes propagate in the ion diamagnetic direction [5, 23–25]. We refer to this mode as the

"ubiquitous mode" in Fig. 1. We note that the ubiquitous mode spans a much larger range of parameter space when $\eta_i = d\ln T_i/d\ln n_i > 0$ [25], and its original definition encompassed all non-resonant modes, regardless of propagation direction [23].

We have compared the linear growth rate spectra from GEM and GS2 for both ITG and TEM cases, using $m_e/m_i = m_e/2m_p$. We obtained close agreement for the ITG case (not shown). The TEM case was compared for six different η_e values in Fig. 4. Agreement is very close, although GEM finds larger growth rates than GS2 for shorter wavelengths $k_y\rho_s > 1$ with $\eta_e \geq 5$. We have increased the number of ballooning periods in GS2 to ten, and have also tested an 8-point, rather than 4-point, gyroaverage in GEM. These tests did not change the growth rate spectra noticeably. GEM was run without its usual low pass filter, which has cutoff $k_y\rho_s \gtrsim 2.2$. Agreement between GS2 and GEM was improved for $k_y\rho_s > 1$, when the electron mass was doubled with $m_e/m_i = m_e/m_p$, suggesting this minor discrepancy might be due integration error in the explicit algorithm used in GEM (GS2 uses a fully implicit linear timestep).

III. NONLINEAR FLUXES

The sudden onset of short wavelengths in the linear GS2 studies when $\eta_e > 1$ suggests that η_e could be an important parameter in nonlinear simulations of TEMs. This motivates us to consider a scan in η_e along a line normal to $\eta_e = 1$, to search for critical behavior as $\eta_e = 1$ is crossed. We have chosen to strongly drive TEMs by intersecting $\eta_e = 1$ at $(R/L_{Te}, R/L_n) = (10, 10)$, so that $R/L_n = 20 - R/L_{Te} = 20/(1+\eta_e)$, to avoid the nonlinear upshift regime [5, 6]. Values chosen for η_e are indicated by the black dots in Fig. 1. Additional values were added as needed.

Nonlinear runs were carried out using both GEM and GS2 flux tube simulations at 16 values of η_e. For GEM, a real-space code, the end-to-end box size was $128\rho_H \times 64\rho_H \times 2\pi qR_0$, with $256 \times 128 \times 32$ spatial gridpoints in the (x, y, z) directions, and 64 particles per cell, where the major radius $R_0 = 1000\rho_H$, and ρ_H is the hydrogen sound speed. For GS2, pseudo-spectral in the binormal directions, 11 k_y values were used with $k_y\rho_s = 0.0, 0.2, 0.4, ..., 2.0$, and 85 $k_x\rho_s$ values were used, ranging from -10.5 to 10.5, for an equivalent box size $70\rho_H \times 90\rho_H \times 2\pi qR_0$ while the nonlinear terms were evaluated using $128\times32\times32$ spatial gridpoints. GS2 runs used 16 energies 32 velocity pitch angles for trapped particles, and 10 pitch angles for circulating particles, with two signs of velocity. GS2 runs typically required 13,000 to 23,000 processor-hours on a 2.3 GHz quad-core AMD Opteron based Cray XT4 computer. GEM simulations in this paper required between 7,680 and 15,000 processor hours on the same system. It is likely that the GS2 simulations are over-resolved in velocity space. The pitch angle grid forces trapped particle bounce points to lie on poloidal angle grid points, fixing the number of trapped particle velocity pitch angles. Run times increased with η_e, and GS2 and GEM were generally within a factor of two.

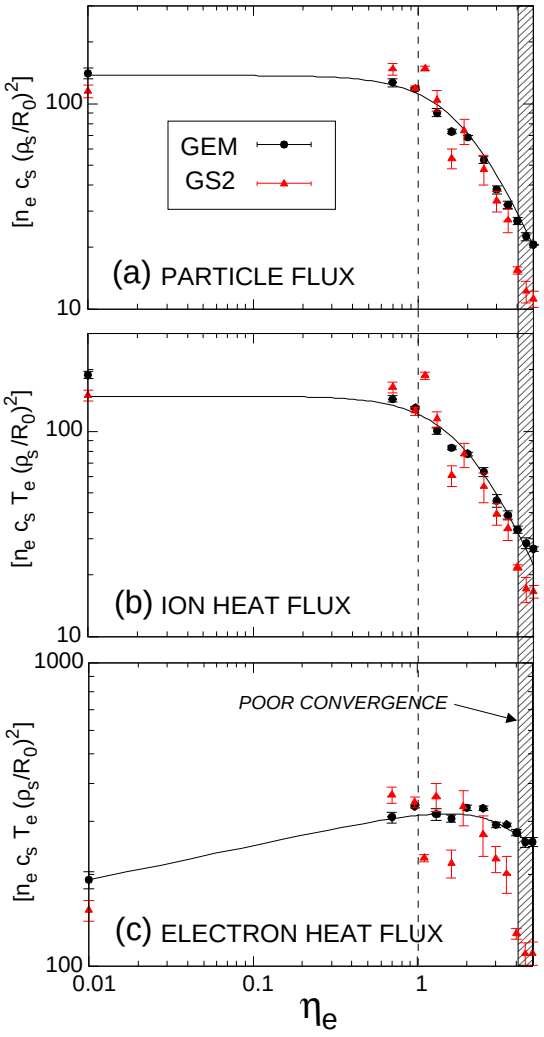

FIG. 5: (Color) Comparison of transport fluxes from nonlinear GEM and GS2 simulations, as a function of η_e: (a) particle flux, (b) ion thermal energy flux, (c) electron thermal energy flux. Error bars are from the GKV lag-window algorithm. Solid line is a bezier smoothed curvefit to GEM data.

Comparison of the fluxes as a function of η_e is shown in Fig. 5. The time-averaged ion fluxes from the two codes very closely agree for $\eta_e < 2$. Relatively small departures can be seen in the particle and ion thermal energy fluxes for the three highest η_e values. The agreement in electron thermal energy flux is less impressive at higher η_e values. Ongoing work will attempt to understand this departure, which could be related to the difference in resolution in the y-direction. For $\eta_e \geq 3$, it is clear that the GS2 runs were not converged. Poloidal wavenumber spectra coalesced to the longest wavelength in the box. Using two different codes made this conver-

gence issue immediately apparent. We have doubled the range of k_x and k_y, and separately doubled the number of k_x and k_y values in GS2. These tests slightly improved convergence, but did not eliminate the problem. Similarly, for $\eta \geq 5$, the GEM fluxes did not saturate. Convergence tests of the same cases with GYRO (see Ref. [26] for general code description) yielded similar results – fluxes did not saturate. However, the problem is physically well-posed. Although the simulations were collisionless, the anti-aliasing (pseudo-spectral) closure in GS2 and GYRO, and the short wavelength filter in GEM, provide effective dissipation at the shortest scales.

It is clear from Fig. 5 that η_e is an important parameter in nonlinear simulations. The variation with η_e mirrors changes in the linear wavenumber spectrum. For $\eta_e < 1$, little variation in fluxes is observed, particularly for particle and ion thermal fluxes. The particle and ion thermal fluxes fall sharply and exponentially with η_e when $\eta_e > 1$. For $\eta_e = 5$, the ion fluxes have fallen an order of magnitude.

We have adapted the analysis package GKV [27] for use with recent GEM versions, and have used GKV to perform the spectral analysis presented. Figure 6 compares the radial and poloidal wavenumber spectral densities of squared electrostatic potential magnitude from GS2 and GEM, for the range of converged η_e values. We have artificially doubled the GEM spectral densities to better compare the shapes of the spectra, which would be consistent with the agreement in transport fluxes, and the likelihood of omitting a factor of two in the reality condition or elsewhere. The agreement is remarkable, except at long radial wavelengths, which approach the box size. Such long wavelengths violate the local flux-tube approximation, and can lead to artifacts of the initial and boundary conditions. The Poisson equation for the zonal potential, $\Phi(k_y = 0, k_x) = -4\pi e(n_i - n_e)/k_x^2$, makes it immediately apparent that small errors $n_i - n_e$ can have a dramatic impact on the potential at long radial wavelengths. Fortunately, long radial wavelengths are physically unimportant on short timescales, given the relatively small flow speeds observed. The more relevant zonal flow shearing rate $\sim k_x^2 \Phi(k_y = 0, k_x)$, which is insensitive to long wavelengths, shows much better agreement between the two codes. The minor departure of GS2 and GEM for $k_y \rho_s \gtrsim 1$ for larger η_e is opposite the departure in the linear spectra shown in Fig. 6.

Figure 7 compares time-averaged statistics for non-zonal fluctuations in GS2 and GEM, as a function of η_e. The two codes agree reasonably well in the eletrostatic potential auto-correlation times, radial and binormal correlation lengths, and half-widths of the binormal correlation functions. Interestingly, the correlation time increases with η_e, consistent with the weakening role of zonal flow shearing. The exponential fall of transport with $\eta_e > 1$ would be consistent with a diffusivity scaling roughly as $r_{\rm corr}^2/\tau_c$, where $r_{\rm corr}$ is nearly constant. To ensure validity of the statistical analysis, the ratio of the duration of the saturated phase in the simulations to the

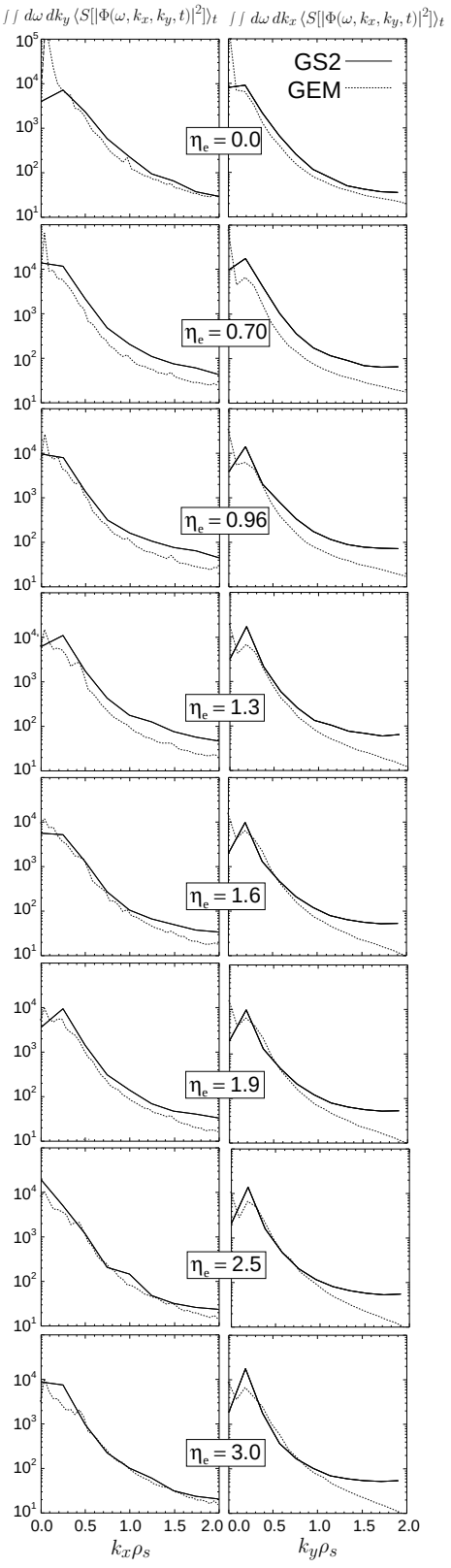

FIG. 6: Comparison of nonlinear GS2 and GEM time-averaged spectral densities (of the squared electrostatic potential), integrated over frequency and one binormal wavenumber. Shown as a function of the remaining binormal wavenumber, $k_x\rho_s$ (left column) and $k_y\rho_s$ (right column), for all η_e values in the scan. The GEM spectral densities have been doubled for comparison. Units are: Φ $[T_e/e\rho_s/R_0]$, freqency ω $[c_s/R_0]$, wavenumber $k_{x,y}$ $[\rho_s^{-1}]$.

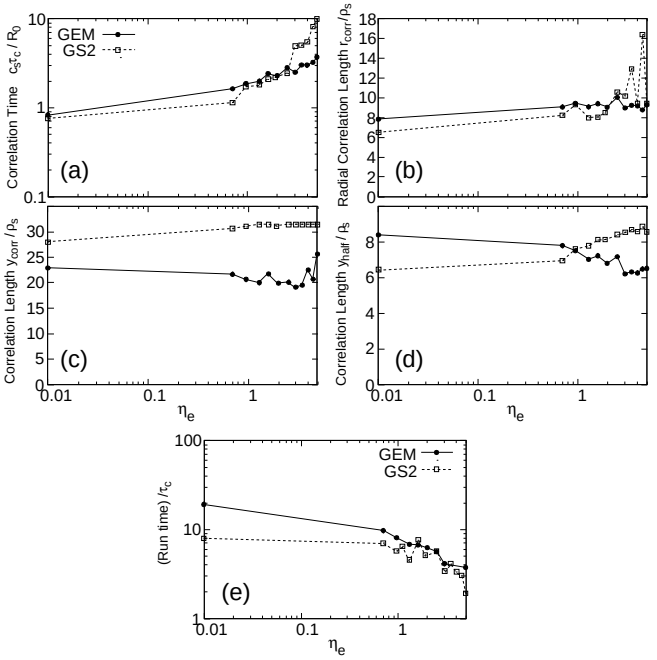

FIG. 7: Comparison of time-averaged statistical analysis for GS2 and GEM runs, as a function of η_e: (a) Correlation time, (b) radial correlation length, (c) binormal (∼poloidal) correlation length, (d) half-width of correlation function in binormal (∼poloidal) direction, and (e) ratio of duration of saturated phase to correlation time.

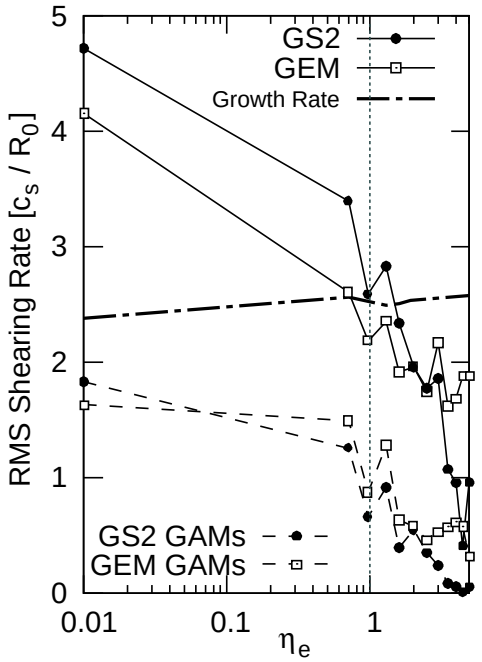

FIG. 8: Comparison of time-averaged zonal flow $E \times B$ shearing rates from GS2 and GEM as a function of η_e. The linear growth rate at $k_y\rho_s = 1$ from GS2 is shown for comparison. Also shown are the shearing rates due to GAMs (frequencies within ±10% of the GAM frequency, $2.345\, c_s/R_0$).

correlation time is examined in Fig. 7(d). GS2 runs are terminated by the onset of a numerical instability (which could possibly be prevented by increasing an implicitness parameter). The largest η_e values are the most challenging for both codes, but fortunately the runs are at least two correlation times long at worst, and twenty at best. Note the flux tube cross-sections significantly exceed the correlation lengths.

IV. ZONAL FLOWS

It has been established that zonal flows are unimportant in TEM saturation at large electron temperature gradients, and are the dominant saturation mechanism in purely density gradient driven cases. However, no explanation for this dependence on plasma parameters has been previously suggested. Here we demonstrate that the role of zonal flows, as well as the transport, in TEM turbulence is sensitive to η_e. Further, as in the linear studies, $\eta_e = 1$ is a critical value, above which zonal flows are relatively unimportant. This suggests, despite little resemblance between the nonlinear and linear wavelength spectra, that the shift of the linear TEM growth rate spectrum to short wavelengths for $\eta_e > 1$ strongly affects the role of zonal flows in TEM saturation.

The time-averaged ratio of zonal flow intensity to the intensity of the time-averaged dominant mode intensity from GS2 and GEM fall sharply above $\eta_e = 1$. At $\eta_e = 5$, this ratio is an order of magnitude smaller. This remains true even though the total time-averaged squared potential and density fluctuations fall exponentially with η_e, as would be expected on the basis of either the zonal density model, or simple mixing length considerations when zonal flows are weak.

The time-averaged rms $E \times B$ shearing rate of the y-averaged zonal flow potential, $\gamma_E = \langle |\partial^2 \bar{\Phi}(x)/\partial r^2|^2 \rangle_t^{1/2}$, from GS2 and GEM nonlinear simulations, is compared to the maximum linear growth rate from GS2, as a function of η_e, in Fig. 8. We have used digital filters to remove spatial scales shorter than the radial correlation length of non-zonal fluctuations, and time scales shorter than the eddy lifetime, as in Ref. [27]. In addition, we have filtered $k_y\rho_s > 1.5$. The rms zonal flow shearing rates decrease with η_e, exceeding the maximum linear growth rate (taken at $k_y\rho_s = 1$) for $\eta_e \lesssim 1$ and falling below it for $\eta_e \gtrsim 1$. Accordingly, zonal flows are unimportant for $\eta_e \gtrsim 1$, consistent with expectation from Fig. 1. Figure 8 also shows the rms shearing rate due to Geodesic Acoustic Modes (GAMs) [17], calculated using a bandpass filter admitting frequencies within ±10% of the GAM frequency. This suggests that shearing by GAMs is generally unimportant for this value of q_0, particularly for $\eta_e > 1$. However, it is remotely possible that the nonlinear excitement of GAMs provides the saturation mechanism for $\eta_e > 1$.

Figure 9 compares the frequency spectra and radial wavenumber spectral densities of the time-averaged rms zonal flow shear as a function of η_e. No particular feature is apparent at the GAM frequency that is consistent in GS2 and GEM. The radial wavenumber spectra are very similar, which is surprising at this level of spectral detail.

V. CONCLUSIONS

We have developed a new linear stability diagram for electron modes as a function of electron temperature and density gradients, based on 2,000 gyrokinetic simulations, separating TEM, ubiquitous, and ETG modes. The most unstable wavenumbers transition sharply to short wavelengths for $\eta_e > 1$, which remain primarily destabilized by trapped electrons. This motivates us to investigate the variation of zonal flows and transport with η_e in a series of nonlinear simulations using both particle-in-cell (the GEM code) and continuum (the GS2 code) methods. The two codes are shown to closely agree except at the largest values of $\eta_e = d\ln T_e/d\ln n_e > 3$, where qualitative agreement is found. Detailed spectral analysis is performed and close agreement is shown in linear growth rate spectra, fluxes, correlation lengths and times, wavenumber spectral densities, zonal flow and GAM shearing rates, and zonal flow shearing rate spectra. Both transport and zonal flows are shown to fall sharply and exponentially as η_e exceeds unity. Fine scale structure appears when $\eta_e \gtrsim 1$, consistent with linear expectations. The observed decreasing transport for $\eta_e > 1$ is loosely consistent with expectation from a simple quasilinear model with mixing length saturation, as the linear spectrum moves to shorter wavelengths, and also with the mode coupling model [10], if k_x of the dominant mode increases with η_e. This will be true if isotropization occurs nonlinearly and $k_x \sim k_y$. Such models become relevant when zonal flows are weak, but do not predict when zonal flows are weak.

Interestingly, the mode coupling models discussed in Sec. I are not directly sensitive to η_e. The maximum linear growth rate is apparently insensitive to η_e in this scan. Sensitivity to η_e in these models is implicit in the variation of the weighted mean k_x and k_y values with η_e, as evident in the linear k_y spectrum, which is not described by the models. The results are also consistent with the adiabaticity of the ions at short wavelengths, where the zonal flow potential $\langle\phi\rangle \sim \langle n\rangle/k_r^2\rho_s^2$ is weaker for a given density perturbation, and secondary instability growth rates are reduced or stable [16, 21]. Thus, even though the zonal flow residual would be near unity [28] for the $k_\perp\rho_i > 1$ typical of temperature gradient driven TEMs, zonal flows are not strongly driven.

Acknowledgments

This work was supported by U. S. DoE contracts DE-FG02-91ER-54108, DE-FG02-91ER-54109, DE-FC02-04ER54784, DE-FC02-08ER54966, the SCIDAC Center for Plasma Edge Simulation, and the DoE SCIDAC Center for the Study of Plasma Microturbulence. Computer simulations using GS2 were carried out on the MIT PSFC Parallel Opteron/Infiniband Cluster and both GEM and GS2 simulations were carried out on the Cray XT4 machine Franklin at the DoE National Energy Research Supercomputer Center. It is a pleasure to thank Dr. Jeff Candy (General Atomics) for initial convergence studies using GYRO at large η_e.

[1] ITER Physics Expert Group on Confinement and Transport and ITER Physics Expert Group on Confinement Modelling and Database and ITER Physics Basis Editors, Chapter 2: Plasma confinement and transport, Nucl. Fusion **39** (12), 2175 (1999).

[2] C. Angioni, L. Carraro, T. Dannert, N. Dubuit, R. Dux, C. Fuchs, X. Garbet, L. Garzotti, C. Giroud, R. Guirlet, F. Jenko, O. J. W. F. Kardaun, L. Lauro-Taroni, P. Mantica, M. Maslov, V. Naulin, R. Neu, A. G. Peeters, G. Pereverzev, M. E. Puiatti, T. Pütterich, J. Stober, M. Valovič, M. Valisa, H. Weisen, and A. Zabolotsky, ASDEX Upgrade Team, JET EFDA Contributors, Phys. Plasmas **14**, 055905 (2007).

[3] T. L. Rhodes, W. A. Peebles, J. C. DeBoo, R. Prater, J. E. Kinsey, G. M. Staebler, J. Candy, M. E. Austin, R. V. Bravenec, K. H. Burrell, J. S. deGrassie, E. J. Doyle, P. Gohil, C. M. Greenfield, R. J. Groebner, J. Lohr, M. A. Makowski, X. V. Nguyen, C. C. Petty, W. M. Solomon, H. E. St. John, M. A. Van Zeeland, G. Wang and. L. Zeng, Plasma Phys. Contr. Fusion **49**, B183 (2007).

[4] I. H. Hutchinson, R. Boivin, F. Bombarda, P. Bonoli, S. Fairfax, C. Fiore, J. Goetz, S. Golovato, R. Granetz, M. Greenwald, S. Horne, A. Hubbard, J. Irby, B. LaBombard, B. Lipschultz, E. Marmar, G. McCracken, M. Porkolab, J. Rice, J. Snipes, Y. Takase, J. Terry, S. Wolfe, C. Christensen, D. Garnier, M. Graf, T. Hsu, T. Luke, M. May, A. Niemczewski, G. Tinios, J. Schachter, and J. Urbahn, Phys. Plasmas **1**, 1511 (1994).

[5] D. R. Ernst, P. T. Bonoli, P. J. Catto, W. Dorland, C. L. Fiore, R. S. Granetz, M. Greenwald, A. E. Hubbard, M. Porkolab, M. H. Redi, J. E. Rice, K. Zhurovich, Alcator C-Mod Group, Phys. Plasmas **11**, 2637 (2004).

[6] D. R. Ernst, N. Basse, W. Dorland, C. L. Fiore, L. Lin, A. Long, M. Porkolab, K. Zeller, and K. Zhurovich, *Proc. 21st Int'l. Atomic Energy Agency Fusion Energy Conference, Chengdu, China, 2006*, Paper No. IAEA-CN-149/TH/1-3 (International Atomic Energy Agency, Vienna, 2007, ISBN 92-0-100907-0). Available at `http://www-pub.iaea.org/MTCD/Meetings/FEC2006/th_1-3.pdf`.

[7] T. Dannert and F. Jenko, Phys. Plasmas **12**, 072309 (2005).

[8] J. Lang, Y. Chen, and S. E. Parker, Phys. Plasmas **14**, 082315 (2007).
[9] M. Hoffman and D. R. Ernst, Bull. Am. Phys. Soc. (2007).
[10] J. Lang, Y. Chen, and S. E. Parker, Phys. Plasmas **15**, 055907 (2008).
[11] J. Anderson, H. Nordmann, R. Singh, and J. Weiland, Plasma Phys. Controlled Fusion **48**, 651 (2006).
[12] P. W. Terry, R. Gatto, and D. A. Baver, Phys. Rev. Lett. **89**, 205001 (2002).
[13] D. A. Baver, P. W. Terry, and R. Gatto, Phys. Plasmas **9**, 3318 (2002).
[14] R. Gatto, P. W. Terry, and D. A. Baver, Phys. Plasmas **13**, 022306 (2006).
[15] L. Chen, Z. Lin, and R. White, Phys. Plasmas **7**, 3129 (2000).
[16] B. N. Rogers, W. Dorland, and M. Kotschenreuther, Phys. Rev. Lett. **85**, 5336 (2000).
[17] P. H. Diamond, S.-I. Itoh, K. Itoh, and T. S. Hahm, Plasma Phys. Contr. Fusion **47**, R35 (2005).
[18] F. Merz and F. Jenko, Phys. Rev. Lett. **100**, 035005 (2008).
[19] J. Li and Y. Kishimoto, Plasma Physics Control. Fusion **44**, A479 (2002).
[20] A. M. Dimits, G. Bateman, M. A. Beer, B. I. Cohen, W. Dorland, G. W. Hammett, C. Kim, J. E. Kinsey, M. Kotschenreuther, A. H. Kritz, L. L. Lao, J. Mandrekas, W. M. Nevins, S. E. Parker, A. J. Redd, D. E. Shumaker, R. Sydora and J. Weiland, Phys. Plasmas **7**, 969 (2000).
[21] W. D. Dorland, F. Jenko, M. Kotschenreuther, and B. N. Rogers, Phys. Rev. Lett. **85**, 5579 (2000).
[22] Y. Chen and S. E. Parker, J. Comput. Phys. **189**, 463 (2003).
[23] B. Coppi and F. Pegoraro, Nucl. Fusion **17**, 969 (1977).
[24] B. Coppi and G. Rewoldt, Phys. Rev. Lett. **33**, 1329 (1974).
[25] B. Coppi, S. Migliuolo, and Y.-K. Pu, Phys. Fluids B **2**, 2322 (1990).
[26] J. Candy and R. E. Waltz, Journal of Comp. Phys. **186**, 545 (2003).
[27] W. M. Nevins and J. Candy and S. Cowley and T. Dannert and A. Dimits and W. Dorland and C. Estrada-Mila and G. W. Hammett and F. Jenko and M. J. Pueschel and D. E. Shumaker, Phys. Plasmas **13**, 122306 (2006).
[28] Y. Xiao and P. J. Catto, Phys. Plasmas **13**, 102311 (2006).

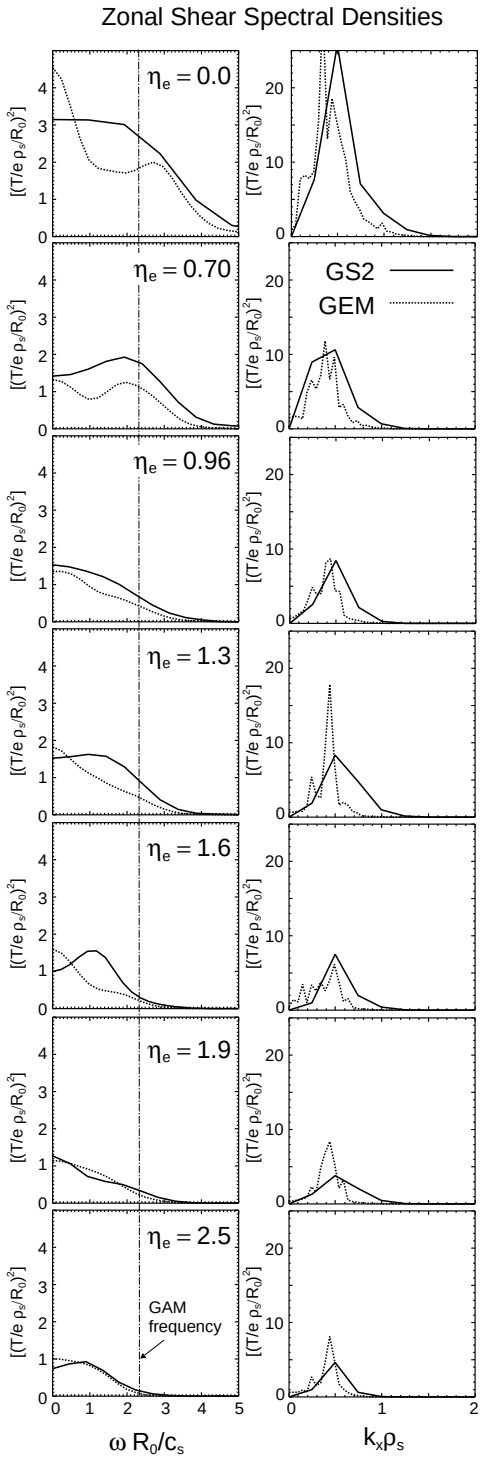

FIG. 9: Comparison of time-averaged spectral densities of the square of the zonal flow $E \times B$ shearing rate, from GS2 and GEM, as a function of frequency (left column) and radial wavenumber (right column), for representative η_e values.